Doctor-blade deposition of quantum dots onto standard window glass for low-loss large-area luminescent solar concentrators

Hongbo Li[†], Kaifeng Wu[†], Jaehoon Lim, Hyung-Jun Song and Victor I. Klimov[*]

Luminescent solar concentrators (LSCs) are envisioned to reduce the cost of solar electricity by decreasing the usage of more expensive photovoltaic (PV) materials and diminishing the complexity of multi-cell PV modules. The LSC concept can also enable unconventional solar-energy conversion devices such as PV windows that can be especially useful in highly populated urban areas. Here we demonstrate low-loss, large-area (up to about $90 \times 30 \, cm^2$) LSCs fabricated from colloidal core/shell quantum dots (QDs) whose optical spectra are tailored so as to minimize self-absorption of waveguided radiation. For improved compatibility with a polymer matrix and enhanced stability, QDs are encapsulated into silica shells, which allows for maintaining high emission efficiencies ($\sim$70% quantum yields) under four-month exposure to air and light, and heat treatments up to 200 °C. The QD/polymer composites are processed into devices using standard doctor-blade deposition onto commercial window glasses. The fabricated semi-transparent devices demonstrate internal quantum efficiencies of more than 10% for dimensions of tens of centimetres.

Luminescent solar concentrators (LSCs) are light-management devices that can serve as large-area sunlight collectors for photovoltaic (PV) cells. An LSC consists of a slab of transparent material (for example, glass or plastic) impregnated or coated with highly emissive fluorophores. Following absorption of solar light impinging onto a larger-area face of the slab, LSC fluorophores re-emit photons at a lower energy and these photons are guided by total internal reflection to the device edges where they are collected by PVs[1]. If the cost of an LSC is much lower than that of a PV cell of a comparable area, and the LSC's efficiency is sufficiently high, then applying these devices one can achieve a considerable reduction in the cost of solar electricity. Application of semi-transparent LSCs can also enable new types of device such as solar or PV windows that could turn currently passive building facades into power generation units[2–6].

Colloidal quantum dots (QDs) have been actively explored in the context of LSC applications that capitalize on QD properties such as widely tunable absorption and emission spectra, high photostability, and solution processability[7,8]. These structures can also be tailored in such a way as to greatly reduce losses to reabsorption (self-absorption) of guided light by using the concept of 'Stokes-shift engineering' implemented via shape control, heterostructuring, or impurity doping. Demonstrated approaches include the use of core/thick-shell 'giant' QDs (g-QDs), Mn- and Cu-doped QDs, type-II heterostructures, and ternary I–III–VI₂ QDs[9–15].

In most of the reported cases, LSC fluorophores have been embedded into polymers such as poly(methyl methacrylate) (PMMA)[9,16,17] or poly(lauryl methacrylate)[12,18] fabricated via bulk polymerization. A common problem in this case is poor compatibility between QDs and polymer materials, which often leads to the degradation of the QD passivation causing the drop in the photoluminescence (PL) quantum yield (QY)[12,17–21]. Another detrimental effect is QD aggregation during the polymerization process, which leads to additional quenching of QD emission due

to inter-dot exciton transfer[22]. Furthermore, the formation of QD clusters increases light scattering leading to a hazy appearance of a QD/polymer slab[16]. Finally, even in a freshly prepared polymer waveguide, unavoidable fluctuations in the refractive index due to fluctuations in the material's density can lead to considerable losses due to scattering[9,23].

One approach to at least partially mitigate the above problems is by replacing an all-polymer LSC waveguide with a layered structure, which comprises a slab of a high-optical-quality glass coated on one or both sides with a polymer/QD composite. The loss to optical scattering in such a structure due to imperfections in the polymer matrix will be reduced in direct proportion to the ratio between the overall waveguide thickness and the thickness of the polymer layer. Here to realize a layered LSC design, we exploit a doctor-blade technique for depositing a thin film of a QD/polymer composite on top of a large-area glass slab. Our LSC emitters are silica-coated, type-I CdSe/Cd$_{1-x}$Zn$_x$S g-QDs, wherein both an electron and a hole are localized within a central CdSe core, while an especially thick Cd$_{1-x}$Zn$_x$S shell, along with an outer silica layer, isolates them from the environment. This helps maintain a high PL QY ($\sim$70%) in a final composite and leads to excellent thermal stability and photostability. We select polyvinylpyrrolidone (PVP) as a matrix material because it can coordinate to the hydroxyl group of a silica shell through the nitrogen atom on the functional pyrrolidone ring[24]. This improves compatibility between QDs and the polymer and helps avoid QD aggregation within the matrix. Using a doctor-blade technique to deposit the QD/PVP composite, we fabricate large-area devices (up to about $90 \times 30 \, cm^2$) in which losses due to self-absorption and scattering at imperfections within the waveguide are almost completely eliminated.

Type-I 'giant' quantum dots
Thick-shell CdSe/CdS g-QDs have been demonstrated to show excellent performance as LSC fluorophores, partially due to a large
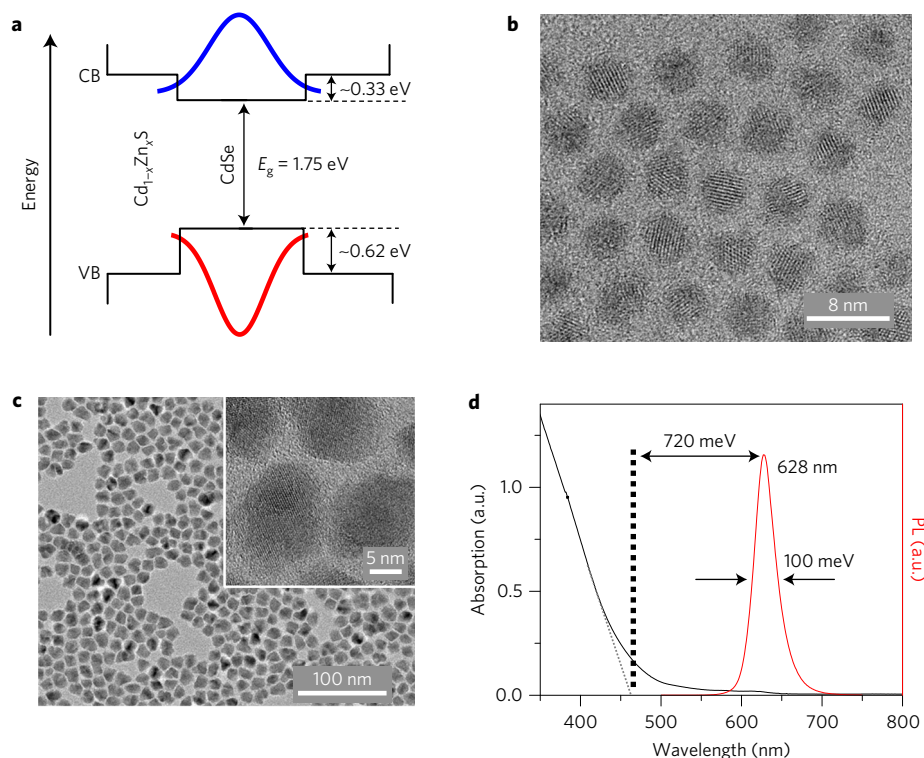

Figure 1 | Thick-shell, type-I CdSe/Cd$_{1-x}$Zn$_x$S g-QDs. a, An approximate structure of a type-I confinement potential in CdSe/Cd$_{1-x}$Zn$_x$S g-QDs with $x \approx 0.4$ (determined from inductively coupled plasma-optical emission spectroscopy)[25]. CB and VB denote the conduction and valence bands, respectively; $E_g = 1.75$ eV is the bulk-CdSe bandgap. Based on the bulk-semiconductor band-edge energies, the conduction- and valence-band offsets at the core/shell interface are ∼0.33 eV and ∼0.62 eV, respectively. **b,** A TEM image of CdSe cores with the 4 nm mean diameter. **c,** A TEM image of core/shell CdSe/Cd$_{1-x}$Zn$_x$S g-QDs. Inset: a high-resolution TEM image of the same QDs. **d,** Absorption (black) and PL (red) spectra of CdSe/Cd$_{1-x}$Zn$_x$S g-QDs. The absorption onset of the shell is at ∼460 nm and the PL peak of the core is at ∼628 nm, indicating a large effective Stokes shift of ∼720 meV.

effective Stokes shift defined by the difference in energies of the CdSe-core PL and the onset of absorption in a 'giant' CdS shell, which serves as a light harvesting antenna[9,18]. It is possible to further capitalize on the beneficial properties of a thick-shell architecture by changing the shell composition from CdS to Cd$_{1-x}$Zn$_x$S[25]. Standard CdSe/CdS g-QDs exhibit a quasi-type-II localization regime[26] wherein the hole is core-confined, while the electron is delocalized across the entire QD volume[27–29]. In this situation, the electron wavefunction can sample defects at the shell surface, which may reduce the PL QY. Further, a nearly bulk-like character of the electron wavefunction limits the range of spectral tunability of both the PL and the onset of strong absorption.

The use of the alloyed Cd$_{1-x}$Zn$_x$S shell can help eliminate the above deficiencies. Specifically, with an appropriate fraction of Zn in the alloy, the conduction-band offset becomes sufficiently large for confining the electron to the CdSe core, which corresponds to the restoration of type-I localization characteristic of CdSe core-only structures but with the benefit of a wide energetic barrier protecting both the electron and the hole from deleterious effects of environment (Fig. 1a). Furthermore, the use of thick-shell, type-I heterostructures extends the range of spectral tunability of both PL (controlled by the core size) and the absorption onset (controlled by the shell composition), and thus, allows for greater flexibility in controlling the effective Stokes shift (Δ_S).

In this study, CdSe/Cd$_{1-x}$Zn$_x$S ($x \approx 0.4$) g-QDs were synthesized by a successive shell growth[25,30] as detailed in the Methods. Transmission electron microscopy (TEM) studies indicate a high monodispersity of CdSe cores (size dispersion <10%), which in the present study have a 4-nm mean diameter (Fig. 1b). At the end of shell growth reaction, the average diameter of the CdSe/Cd$_{0.6}$Zn$_{0.4}$S

g-QDs is 12.0 nm (∼15% size dispersion; Fig. 1c and Supplementary Fig. 1a), indicating that the average shell thickness is 4.0 nm. The final particles have irregular shapes that are typical of thick-shell structures (Fig. 1c)[25]. According to high-resolution TEM images (inset of Fig. 1c), they do not exhibit any apparent defects such as misfit dislocations, which results in a fairly high PL QY of ∼70%. The PL peak is at ∼628 nm and the onset of absorption due to the thick alloyed shell is at ∼460 nm (Fig. 1d). These values correspond to Δ_S of ∼720 meV, which is sufficiently large to considerably reduce self-reabsorption of emitted light, a key requirement for an LSC fluorophore[9,18].

Encapsulation of quantum dots into silica shells

As fabricated, the CdSe/Cd$_{1-x}$Zn$_x$S g-QDs are hydrophobic and not compatible with polar solvents used in the fabrication of QD/polymer composites. To change the surface of QDs to hydrophilic, we encapsulate them into silica shells. Previously, this approach has been successfully applied to both spherical semiconductor particles[31–33] as well as nanocrystals of other shapes including nanorods, tetrapods and nanoplatelets[34,35].

While allowing for good solubility in polar solvents, a common issue associated with silica overcoating is a complete or partial PL quenching. The most successful demonstrated procedures, which allowed for retaining up to ∼40% of the original PL QY, involved an oil-in-water micro-emulsion reaction[31,32,36] or very slow silanization of the QDs to replace their surface ligands by partially hydrolysed tetraethyl orthosilicate (TEOS)[37]. In the present work, we have explored the first of these approaches (see Methods for details). It allows for tuning the silica-shell thickness (H) by adjusting relative amounts of QDs and TEOS in the synthesis. Under optimized
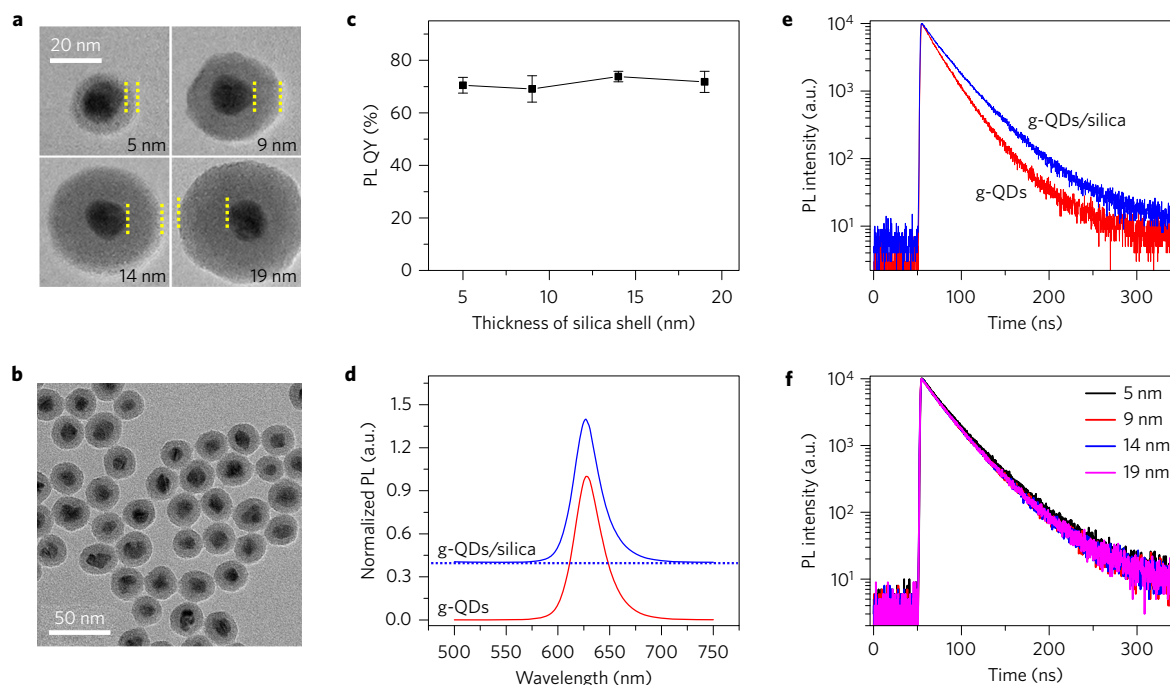
Figure 2 | Silica-coated g-QDs. a, TEM images of individual CdSe/Cd$_{1-x}$Zn$_x$S g-QDs overcoated with a silica shell of different thicknesses (indicated in the figure). **b**, A TEM image of a large-area view of silica-coated g-QDs with the mean silica-shell thickness of 5 nm. **c**, The emission efficiency of silica-coated g-QDs in ethanol as a function of shell thickness. Error bars represent a standard deviation in PL quantum yields from three independent measurements. **d**, The PL spectra of uncoated (red) and silica-coated (blue; 5-nm shell thickness) g-QDs dissolved in toluene and ethanol, respectively. **e**, Comparison of PL dynamics of uncoated (red) and silica-coated (blue) g-QDs (same solvents as in **d**). **f**, The PL decay in silica-coated g-QDs as a function of shell thickness.

conditions, H can be varied from 5 nm to 19 nm (Fig. 2a). In our LSCs, we use QDs overcoated with ∼5-nm-thick shells, which corresponds to the overall particle size of 22.5 ± 2.3 nm (Fig. 2b and Supplementary Fig. 1b). The TEM measurements indicate that in the majority of the composite particles (>99%), the QD is located at the centre of the structure (Fig. 2b). Also, only rarely we observe instances of multiple dots residing within the same silica shell or QDs located at the silica-shell surface, while these problems have been common in previous reports on silica-coated dots[36].

Furthermore, whereas in all previous studies, overcoating with silica has resulted in at least partial PL quenching[37], in the case of our thick-shell, type-I g-QDs, this procedure does not lead to any losses in the PL intensity (Supplementary Fig. 2), and for all studied shell thicknesses, the QDs preserve the original (∼70%) PL QY (Fig. 2c). In addition, encapsulation into silica shells does not modify either the PL peak position or spectral profile (Fig. 2d), and does not considerably alter PL dynamics (Fig. 2e,f). A small increase in the PL 1/e-decay time (from 19.5 ns to 26.2 ns) can be explained by the difference in the dielectric constants of ethanol (used with silica-coated dots) and toluene (used with uncoated dots); see Supplementary Note 1. As elaborated in the Methods (see also Supplementary Fig. 3), deposition of a silica shell also helps suppress PL losses due to energy transfer in QD aggregates that are often formed during the preparation of QD/polymer composites. All of these observations indicate that the silica shell does not perturb the emitting state of these thick-shell, type-I g-QDs.

An important benefit of silica overcoating is a significant improvement of long-term photo- and thermal stability of the QDs compared with uncoated dots. For example, silica-coated dots retain ∼85% of the original PL QY after 4 months of exposure to air and room light, versus ∼23% in the case of uncoated QDs (Fig. 3a). A high level of stability of silica-coated QDs is also indicated by 'accelerated-ageing' studies (see Methods and Fig. 3b) conducted in an air-free environment (N$_2$ atmosphere). According to these tests,

the PL QY drops only by ∼9% after 200 h of exposure to 462-nm light with an intensity that corresponds to the acceleration factor of 247. This translates into 5.6 years of continuous exposure to direct sunlight or ∼14 years of outdoor lifetime if one accounts for a standard day–night cycle.

Silica-coated dots also show a high level of thermal stability (see Methods). Specifically, no appreciable change in the PL efficiency is observed after heat treatment at 200 °C for 30 min in air, while a similar treatment of uncoated QDs results in an ∼60% loss of their PL intensity (Fig. 3c). This remarkable thermal and long-term photostability of the silica-coated, type-I g-QDs indicates that these nanostructures are suitable not only for proof-of-principle device demonstrations but also for applications in real-life technologies where the material's stability is one of the key requirements.

Fabrication of thin-film LSCs

A common method for fabricating LSCs has been bulk polymerization of precursors containing monomers and QDs[9,12,18]. These all-polymer devices, however, suffer from considerable optical losses due to scattering at imperfections within the polymer matrix[9,11,23]. As discussed earlier, the effects of scattering can be reduced by replacing an all-polymer waveguide with a layered structure, which comprises a high-optical-quality glass slab coated with a thin layer of the QD/polymer composite. To implement this device architecture, we apply a doctor-blade deposition technique[38]. This method is highly versatile and allows for fabricating highly uniform films with a precisely controlled thickness on flat substrates of virtually any dimensions and compositions[38,39].

In the present work, we use both manual and automated versions of the doctor-blade technique (see Methods). For quantitative studies of the LSC performance, we use square-shaped glass slabs with the thickness (D) of 1.59 mm and the side length (L) from 2.54 to 20.32 cm (1 to 8 inches) (Fig. 4a and Supplementary Fig. 4). The thickness (d) of the fabricated QD/polymer layer is ∼50 μm.
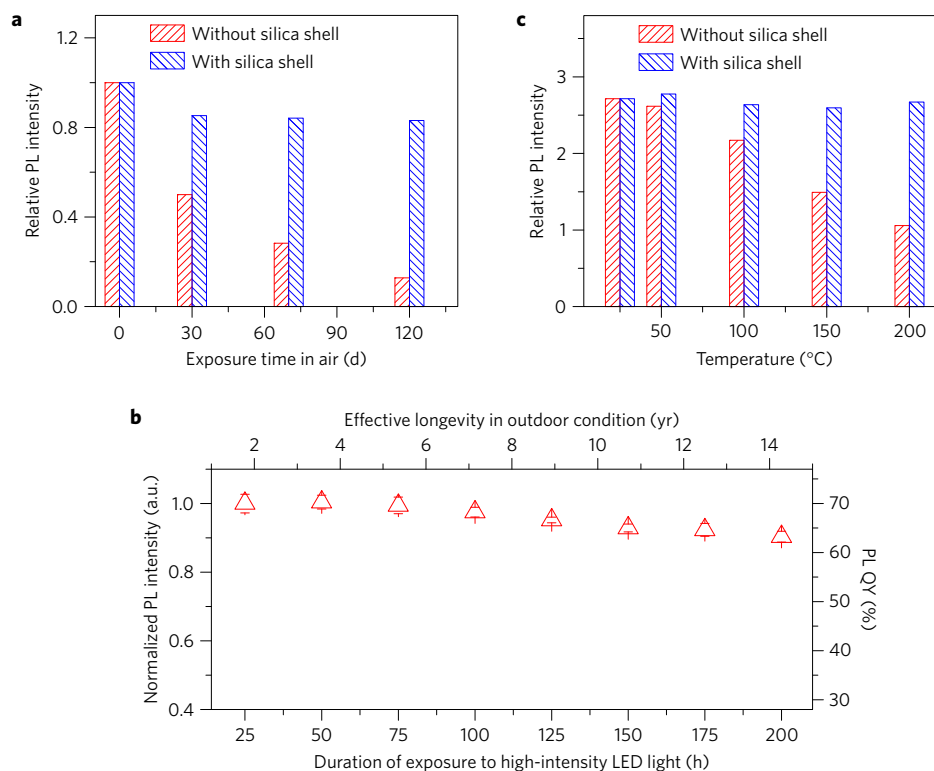
Figure 3 | Tests of photostability and thermal stability of silica-coated and uncoated g-QDs. a, PL intensity of spin-coated films of silica-coated (H = 5 nm; blue bars) and uncoated (red bars) g-QDs exposed to air and room light as a function of time over the four-month period. **b**, An accelerated stability test on a film of drop-cast silica-coated g-QDs in a N_2 atmosphere. The excitation source is a 462-nm LED with an intensity of 1.57 W cm^{-2}, which corresponds to the acceleration factor of 247. Error bars represent a standard deviation from three independent measurements. **c**, Relative PL intensity as a function of heat-treatment temperature for g-QDs without silica shells (red bars) and silica-coated dots (blue bars) during thermal stability tests.

The geometric gain factor of these devices (the ratio of the areas of the front surface and device edges), $G = L/[4(D + d)]$, varies from 4 to 32. In addition, we have used large-area rectangular pieces of commercial glass (30.5 × 91.4 cm^2) to demonstrate real-life, window-size LSCs (Fig. 4b). Regardless of the size, the fabricated devices are highly luminescent and exhibit a strong wave guiding effect as indicated by bright emission emerging from the slab edges under both sunlight illumination (Fig. 4c) and weak ultraviolet illumination (Fig. 4d).

Evaluation of LSC performance

As per our earlier discussion, thin-film LSCs prepared on glass slabs are expected to exhibit much weaker light scattering than all-polymer LSCs. A typical signature of optical scattering is a low-energy tail in absorption spectra extending past the band edge into the intra-gap region. This tail is absent in our samples (Fig. 4e), and at energies below the QD bandgap, the absorption spectrum exhibits only a small constant offset (optical density of ~0.04) due to light reflection from the front and back LSC surfaces (~8% reflectivity).

A considerable reduction in optical losses compared with all-polymer devices is also indicated by studies of PL attenuation as a function of propagation length in the LSC waveguide (Fig. 4f). In previous measurements of LSCs made by bulk polymerization of CdSe/CdS g-QDs/PMMA composites, the PL loss on the distance of ~10 cm was about 50%, which was assigned primarily to scattering within the polymer matrix[9]. In our thin-film devices, the loss is only ~15% on the same propagation distance (Fig. 4f), indicating the expected suppression of light scattering.

The reduced scattering losses result in a considerable improvement in the performance of our thin-film devices compared with previously demonstrated LSCs based on similar thick-shell

g-QDs. To characterize fabricated LSCs, we use a 'fibre-in-fibre-out,' integrating-sphere set-up (Fig. 5a and Supplementary Fig. 4) and apply an approach that is similar to that utilized previously in measurements of PL QYs of thin-film and powder samples[40,41]. The excitation source is a 405-nm light-emitting diode (LED). All studied LSCs have an optical density of 0.6 at 405 nm, which corresponds to the transmission coefficient (T) of 25%. Due to constraints imposed by the size of our integrating sphere, the largest LSCs tested in these measurements are characterized by L = 10.16 cm. The details of the LSC characterization can be found in the Methods.

In our experiments, we quantify the total LSC PL intensity (I_{LSC}) and the PL loss due to emission into the escape cone (I_{loss}) obtained after masking the LSC edges with a black tape (Fig. 5b and Supplementary Fig. 4). The difference between I_{LSC} and I_{loss} yields the intensity of 'useful' emission emerging from the LSC edges (I_{edge}). Dividing I_{edge} by I_{LSC}, we obtain the edge-emission efficiency (η_{edge})[42]. To quantify the total PL QY of the LSC ($\eta_{PL,LSC}$), we divide I_{LSC} by the total number of absorbed pump photons obtained from the difference in the LED emission spectra measured with and without the LSC in the integrating sphere (Supplementary Fig. 5a).

As displayed in Fig. 5c, both $\eta_{PL,LSC}$ and η_{edge} decrease with increasing the LSC length. Specifically, $\eta_{PL,LSC}$ drops from 65.4% to 55.0% (~16% relative difference) when L increases from 2.54 to 10.16 cm (Fig. 5c), which is mostly a result of increasing losses due to reabsorption followed by non-radiative recombination[18]. Another manifestation of reabsorption is the redshift of edge-detected PL versus the PL escaping through the front and back LSC faces, which increases with the device size (Supplementary Fig. 5).

On the basis of the 'intrinsic' PL QY measured on dilute QD solutions (η_{PL} = 69.3%), and the above measurements of QYs of the LSCs, we can estimate the average number of reabsorption
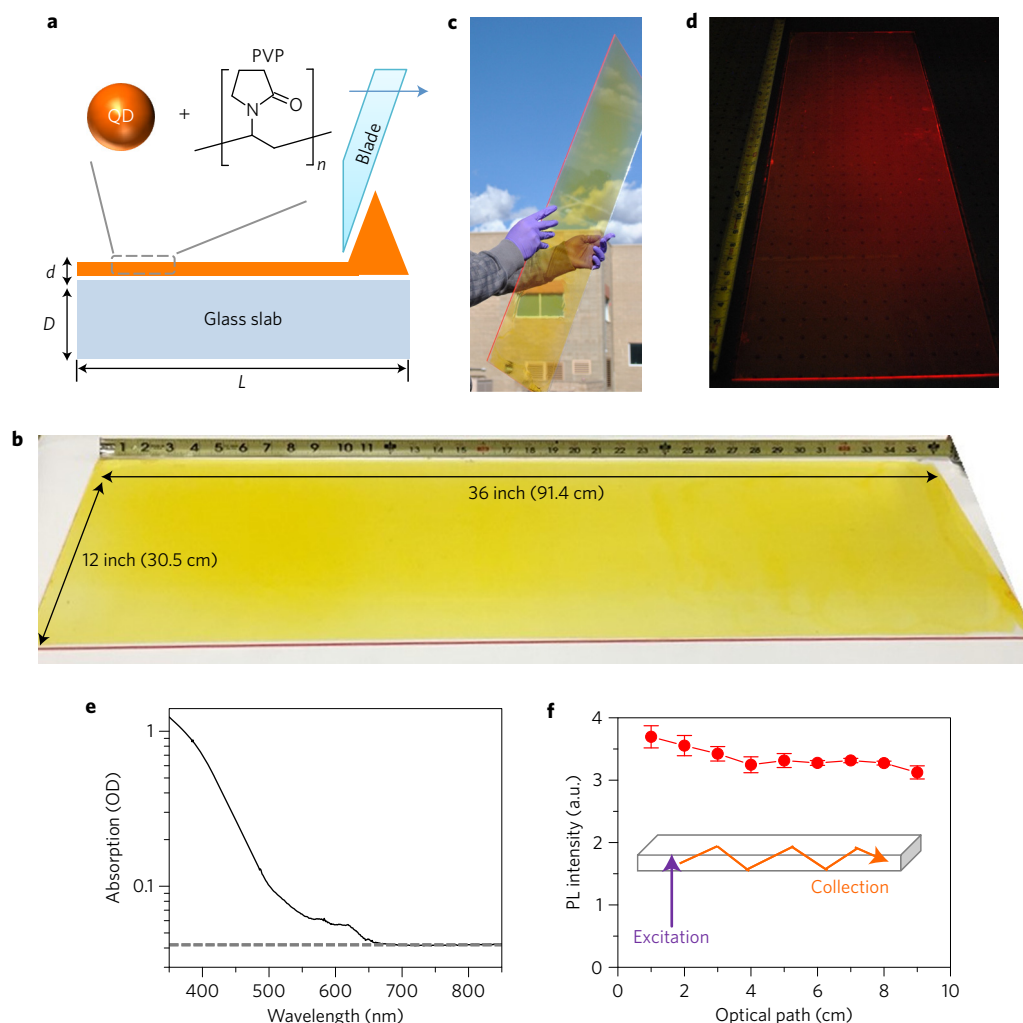
Figure 4 | Fabrication of thin-film LSCs by a doctor-blade technique. a, A schematic representation of thin-film deposition using a doctor-blade method. The g-QD/PVP/ethanol slurry is placed behind the instrument blade and spread onto the glass slab by laterally translating the blade over the substrate. **b**, A photograph of a large-area LSC ($91.4 \times 30.5\ cm^2$ or $36 \times 12\ inch^2$) fabricated by the doctor-blade method. **c,d**, The same LSC as in **b** under sunlight (**c**) and weak UV illumination (**d**). **e**, An absorption spectrum of a fabricated thin-film LSC. **f**, Spectrally integrated intensity of PL from the LSC edge as a function of separation of the excitation spot and the edge (inset). Error bars represent a standard deviation from three independent measurements.

events experienced by the first-generation PL photons during their propagation in the waveguide ($N_{re\text{-}abs}$). Following each reabsorption event, the probability of recovering the photon is defined by η_{PL}. Hence, the LSC PL QY can be related to η_{PL} by $\eta_{PL,LSC} = (\eta_{PL})^{1+N_{re\text{-}abs}}$, which yields $N_{re\text{-}abs} = [\ln(\eta_{PL,LSC})/\ln(\eta_{PL}) - 1]$. Using this expression, we obtain that $N_{re\text{-}abs}$ is approximately 0.16, 0.38, 0.48 and 0.63, for devices with L = 2.54, 5.08, 7.62 and 10.16 cm, respectively. It is expected that $N_{re\text{-}abs}$ should scale directly with the device lateral dimensions. In agreement with these expectations, the scaling of $N_{re\text{-}abs}$ (1.0:2.4:3.0:3.9) closely follows that of the LSC sizes (1:2:3:4). This confirms that the main loss mechanism in these devices is not scattering within the waveguide but weak reabsorption by the QDs.

The efficiency of edge emission (η_{edge}) shows a faster drop with increasing device size (~32% relative decrease as L increases from 2.54 to 10.16 cm) than $\eta_{PL,LSC}$ (Fig. 5c). This behaviour is easily understood if one takes into account that in addition to non-radiative losses, η_{edge} is affected by 'randomization' of photon propagation direction during each reabsorption or scattering event, which leads to additional losses via emission into the escape cone. The LSC internal quantum efficiency ($\eta_{int} = \eta_{PL,LSC}\,\eta_{edge}$; see Methods) shows the same LSC-size dependence as η_{edge}, and it

decreases from 41.6% to 23.9% as L increases from 2.54 to 10.16 cm (Fig. 5c). Accounting for the LSC absorptance at the excitation wavelength (η_{abs}; see Methods), the external quantum efficiency ($\eta_{ext} = \eta_{abs}\,\eta_{int}$) for the smallest and the largest studied devices is 30% and 17%, respectively (Fig. 5c). Further, taking into account the geometric gain factor, we find that the optical concentration factor ($C = G\eta_{ext}$) achieved with these devices is from 1.2 to 2.7.

Next we analyse these measurements using an analytical model of planar LSCs of ref. 5, which was benchmarked against Monte Carlo ray-tracing simulations[9,18,21], and further validated by experiments on QD-solution-based devices. Applying this formalism to the fabricated LSCs (Supplementary Note 2), we can accurately describe the results of our measurements for η_{ext} and C; compare symbols (experiment) and lines (calculations) in Fig. 5d.

To validate the results of optical measurements of LSC efficiencies as well as theoretical modelling, we have also conducted electro-optical studies using coupled LSC–PV devices measured under natural outdoor illumination (Supplementary Notes 3 and 4). In these experiments, we use flexible amorphous silicon (a-Si) modules attached to one of the LSC edges with an index-matching polymer adhesive. By comparing short-circuit currents of the stand-alone PV and the LSC–PV system (Supplementary Fig. 7a), we obtain that
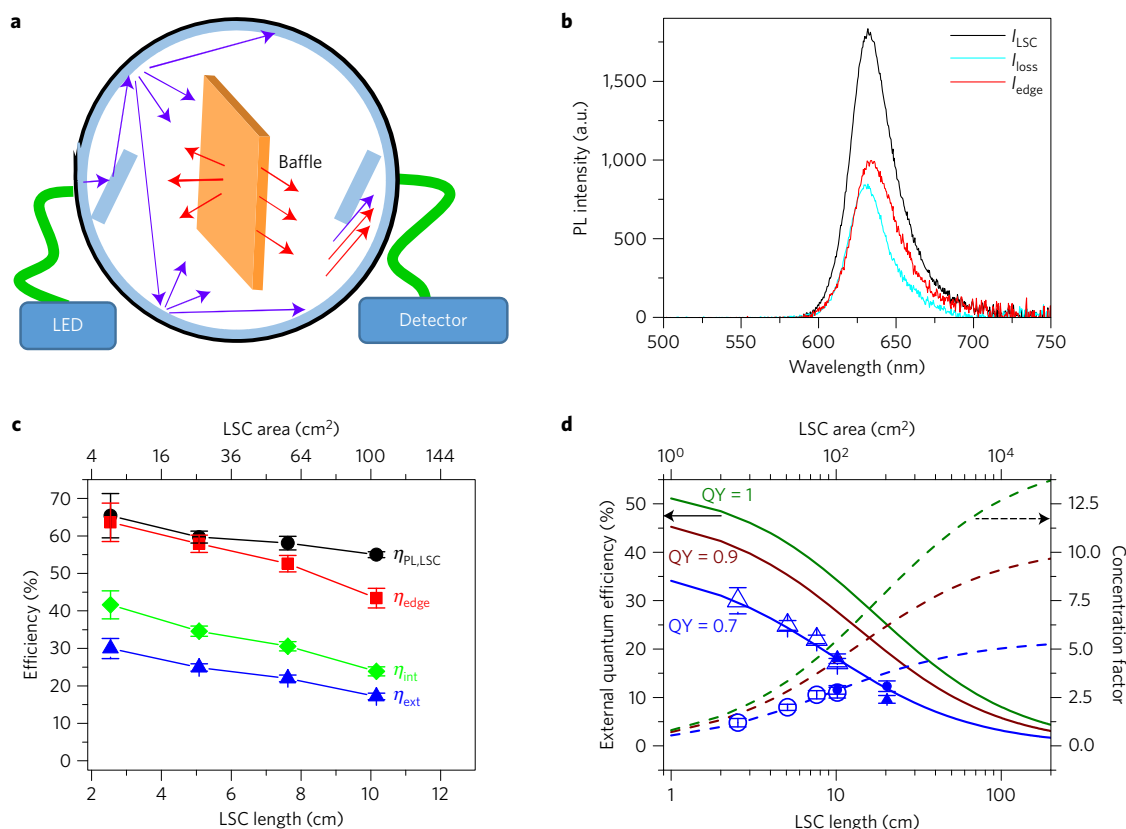
Figure 5 | Evaluation of the performance of fabricated devices. a, A schematic of a fibre-in-fibre-out, integrating-sphere set-up used to quantify various efficiencies of fabricated LSCs. The sample is excited by a 405-nm LED coupled to the input fibre. A tested device is shielded from direct exposure to incident LED light by a baffle, which leads to diffuse illumination of the LSC (blue arrows); this is similar to a real-life situation of illumination with ambient sunlight. The second baffle shields the output of the integrating sphere to eliminate errors arising from a considerable difference in angular distributions of light emitted from the LSC edges and the light leaving the LSC through the escape cone (red arrows). **b**, The spectra of total LSC emission measured for the unmasked device (black) and the face emission obtained for the device with masked edges (cyan); the LSC size is 5.08×5.08 cm^2. The edge-emission spectrum (red) is obtained by subtracting the above two spectra. **c**, The LSC PL QY ($\eta_{PL,LSC}$; black circles) and the edge-emission efficiency (η_{edge}; red squares) of fabricated devices as a function of their size. The product of $\eta_{PL,LSC}$ and η_{edge} yields the internal quantum efficiency of the LSC (η_{int}; green diamonds). Multiplied by the LSC absorptance, η_{int} is converted into the external quantum efficiency (η_{ext}; blue triangles). **d**, The measured η_{ext} (open blue triangles) is accurately described using the calculations for the PL QY of 70% (blue solid line). The open blue circles and the dashed blue line are, respectively, measured and calculated (η_{PL} = 70%) optical concentration factors (C). The values of η_{ext} (solid blue triangles) and C (solid blue circles) for 10.16 cm and 20.32 cm LSCs derived from electro-optical measurements. The brown and green lines show calculated η_{ext} (solid) and C (dashed) for, respectively, PL QYs of 90% and 100%. Error bars in **c** and **d** represent a standard deviation from three independent measurements.

the internal quantum efficiency of the LSC with $L = 10.16$ cm is 0.21, which is very close to both the efficiency obtained from the integrating-sphere measurements ($\eta_{int} = 0.24$) and η_{int} predicated by the theoretical model ($\eta_{int} = 0.25$); see Fig. 5c,d. A close correspondence between all three values indicates that both optical and electro-optical methods allow for accurate evaluation of the LSC performance.

We also apply the above PV method to the 20.32-cm device, which could not be characterized with the integrating sphere due to its size limitations. Based on the PV-based measurements (Supplementary Note 4 and Supplementary Fig. 7b), η_{int} of this LSC is 0.15; this is again in excellent agreement with the value obtained from the model ($\eta_{int} = 0.16$), suggesting that our theoretical analysis should allow for accurate projection of the performance of larger devices based on the measurements of LSCs of smaller sizes.

On the basis of the calculations, with the currently available QDs and the same device architecture as in the present study, we should be able to maintain high external efficiencies of more than 10% for LSC lengths up to 25 cm, which should also allow for pushing the concentration factor to more than 4. Even with a large, window-size

LSC ($L = 100$ cm), η_{ext} is still about 3% ($C \approx 5$). A further boost in the LSC performance can be obtained by improving the PL QY of the QDs. As illustrated in Fig. 5d, increasing η_{PL} to 90% will lead to almost doubling the external efficiency ($\eta_{ext} \approx 5.8\%$) of the 100-cm devices. A further increase to 8% should be possible with $\eta_{PL} = 100\%$.

Performance comparison and cost-efficiency analysis

The performance characteristics of our devices compare favourably to those of the highest-efficiency QD-LSCs reported in the literature, especially in the case of larger-area structures (see Supplementary Fig. 6 and Supplementary Table 1). An important metric of an LSC, which defines its maximum practical size, and thus the amount of harvested light, is the internal quantum efficiency. On the basis of this metric, all our larger-area devices ($L^2 > 25$ cm^2) are either on a par with or superior to LSCs reported in the literature (see Supplementary Fig. 6). For example, a ~28-cm^2 device of ref. 9 fabricated using CdSe/CdS g-QDs and bulk-polymerized PMMA exhibited η_{int} of ~10% (limited primarily by scattering losses in the polymer waveguide) versus ~34% in our thin-film LSCs of similar sizes (~26 cm^2). In the case of larger-area LSCs (>100 cm^2),

one of the best-performing literature devices based on CuInSe$_{2-x}$S$_x$ QDs showed η_{int} of ~17% for the 144-cm^2 area[12]. With our thin-film approach, we are able to realize a comparable performance (η_{int} = 15%) with a considerably larger, 413-cm^2 LSC.

One of the motivations for the development of the LSC technology has been a potential reduction in the cost of solar electricity by using LSCs as inexpensive, high-efficiency sunlight collectors for traditional solar cells. According to our cost/efficiency analysis (Supplementary Notes 5 and 6), a break-even point for the LSC technology is realized when the overall LSC external quantum efficiency for the entire solar spectrum ($\eta_{s,ext}$) is equal to $\gamma(f + G^{-1})$, where f is the ratio between the per square metre costs of an LSC and a PV module and γ is the constant related to the difference in the angular dependence of the LSC and PV efficiencies and the effect of spectral reshaping of incident radiation by the LSC (both effects play a favourable role in LSCs; see Supplementary Note 6 and Supplementary Fig. 8); for the parameters of the studied LSCs and a standard, high-efficiency silicon PV module, $\gamma = 0.36$ (Supplementary Note 6). Further, based on our LSC cost estimations, in the case of mass production of the QDs, $f = 0.08$ (Supplementary Note 5 and Supplementary Table 2). If we consider a device with the geometric gain factor $G = 10$, we obtain that QD-LSCs can reach the break-even point when $\eta_{s,ext} = 6.5\%$. The quantity $\eta_{s,ext}$ can be expressed as the product of η_{int} and the LSC absorptance across the entire solar spectrum ($\eta_{s,abs}$). For our devices, $\eta_{s,abs}$ is about 6% and for $G = 10$, $\eta_{int} = 31\%$. These values yield $\eta_{s,ext}$ of about 1.9%, which is about a factor of 3.4 below the 'break-even' efficiency (see Supplementary Fig. 9a). It is obvious that the main limitation of the present devices is low absorptance. If it is increased to 20% (by, for example, lowering the absorption onset and increasing a QD concentration in a film), $\eta_{s,ext}$ will be boosted to 6.3%, which is very close to the break-even point. A further improvement is possible by increasing the QD PL QY. The boost in η_{PL} from 70% to 90% will improve $\eta_{s,ext}$ by a factor of ~1.7 (Supplementary Fig. 9b)[5], bringing it to ~10.4%. At this point, an LSC–PV system can, in principle, provide ~40% cost saving compared with stand-alone PV modules.

Conclusions

We have demonstrated large-area (up to about 90 × 30 cm^2), low-loss, thin-film LSCs that are based on type-I CdSe/Cd$_{1-x}$Zn$_x$S g-QDs, encapsulated into silica shells, and deposited onto glass slabs using a doctor-blade technique. The use of silica coating improves the compatibility of the QDs with a polymer matrix and greatly enhances their stability, as verified by a four-month photo-exposure test along with tests for thermal stability at temperatures up to 200 °C. The doctor-blade thin-film fabrication technique presented in this work is highly versatile and can be applied to any mutually compatible QD/polymer pairs including both polar and nonpolar systems. This method does not require any special substrates and can be applied to standard window glass or any other flat surface made of an arbitrary material. Importantly, in the case of the deterioration of the QD-LSC layer, the substrate can be easily re-used by replacing an old QD film with a new one. The use of this inexpensive and highly scalable technique may represent a practical route to real-life applications of QD-LSCs in both semi-transparent solar windows and high-concentration collectors of sunlight supplementing existing PV cells.

Methods

Materials. Cadmium oxide (CdO, 99.999%), zinc acetate (Zn(OAc)2, 99.99%), trioctylphosphine (TOP, 97%), sulfur (S, 99.999%), and selenium (Se, 99.999%) were purchased from Strem Chemicals. Myristic acid (99%), oleylamine (70%), oleic acid (90%), 1-octadecene (90%), tetraethyl orthosilicate (TEOS, distilled before use), ammonium hydroxide solution (NH$_4$OH, 28.0-30.0 wt% NH$_3$ basis, diluted to 20 wt%), IGEPAL CO-520, anhydrous ethanol, cyclohexane, toluene and polyvinylpyrrolidone (PVP, average molecular weight 40,000) were purchased

from Sigma-Aldrich. All chemicals were used without further purification, unless specified.

Synthesis of thick-shell CdSe/Cd$_{1-x}$Zn$_x$S g-QDs. The synthesis of g-QDs followed previously published recipes[25,30]. Briefly, the zinc blende CdSe cores with a 2-nm mean radius were prepared by rapidly injecting 0.5 mmol of TOPSe into a mix of 1 mmol of cadmium myristate and 15 ml 1-octadecene. The fabricated CdSe cores were reacted without purification with 2 ml of 0.5 M cadmium oleate, 4 ml of 0.5 M zinc oleate, and 1.5 ml of 2 M n-trioctylphosphine/sulfur repeatedly added at 300 °C. This procedure resulted in the formation of the Cd$_{1-x}$Zn$_x$S alloyed shell with the thickness controlled by the duration of the reaction. The alloyed shell growth was monitored by taking reaction aliquots at different time intervals and analysing them with a TEM (for morphological information) and inductively coupled plasma atomic emission spectroscopy (for compositional information). In the QD samples used in the present study the mean shell thickness was 4.0 nm and $x \approx 0.4$. The detailed overview of structural and optical properties of these QDs can be found in ref. 25.

Deposition of a silica shell. To overcoat the synthesized QDs with silica shells we applied a micro-emulsion reaction[31,32]. Briefly, 100 ml of cyclohexane as a solvent and 12 g of IGEPAL CO-520 as a surfactant were mixed at room temperature. Five hundred milligrams of g-QDs dispersed in 3 ml of toluene (concentration of the g-QDs was estimated to be about 2.7 × 10^{-8} mol l^{-1}) were introduced into the above mixture, and then 2 ml (9 mmol) of TEOS was added. The reaction was initiated by adding 3 ml of ammonium at the rate of 1 ml min^{-1} and then it was allowed to proceed for 40 h. During the coating process, the PL intensity was monitored as a function of reaction time (Supplementary Fig. 2). After purification, the silica-coated g-QDs could be readily dispersed in polar solvents such as water or ethanol. The above experimental conditions resulted in a silica-shell thickness of 5 nm. The shell thickness could be controlled by adjusting the relative amounts of g-QDs and TEOS.

Evaluation of effects of energy transfer. The deposition of a silica shell helps suppress PL losses in dense QD assemblies such as QD clusters that are often formed during the preparation of QD/polymer composites. In the case of QD clustering, a photo-injected exciton can undergo multiple steps of energy transfer (ET) driven by near-field dipole–dipole interactions between proximal QDs. Because of this process, the exciton can sample non-radiative centres not just in one but multiple QDs, which leads to the decrease of the PL QY compared with the case of dilute solutions where QDs are isolated from each other.

To investigate the effect of silica overcoating on PL quenching due to ET, we study close-packed, spin-cast films of the QDs without and with silica shells (5-nm shell thickness). The ET in samples of CdSe/Cd$_{0.6}$Zn$_{0.4}$S g-QDs is expected to be considerably suppressed compared with core-only or thin-shell samples due to the presence of thick shells that increase the separation between emitting CdSe cores. Indeed, such suppression has been recently documented in ref. 25. However, while being reduced in efficiency, ET is still clearly manifested in samples prepared without silica shells as a small but measurable redshift (3 nm or 10 meV) of the PL peak versus that in the solution sample (Supplementary Fig. 3a, bottom). This is indicative of exciton migration from smaller to large dots, as has been observed in numerous previous studies starting from the first observation of this effect in QD films[43]. In contrast, in films of silica-coated QDs, the PL spectrum is indistinguishable from that of the solution sample (Supplementary Fig. 3a, top), indicating a nearly complete suppression of ET.

This assessment is confirmed by the evaluation of the PL efficiencies measured by an integrating-sphere method. On the basis of these measurements, the PL QY of the CdSe/Cd$_{0.6}$Zn$_{0.4}$S g-QDs without silica coating is quenched by ~38% in close-packed films compared with QD solutions (Supplementary Fig. 3b). On the other hand, the emission efficiency of films of silica-coated dots is virtually the same as that of dots in solution (Supplementary Fig. 3b).

Photostability tests under standard room light. In tests of photostability, spin-cast films of silica-coated (5-nm shell thickness) and uncoated QDs were exposed to air under room lights, and their PL intensity was monitored over a period of time of four months. The film of uncoated QDs showed a monotonic decrease in the PL intensity with time and after 4 months it retained only ~23% of the original PL QY (Fig. 3a). In contrast, the film of silica-coated QDs showed an ~15% PL intensity loss during the first month and then exhibited a nearly constant PL intensity (Fig. 3a), such that ~85% of the original PL QY was preserved at the end of the four-month test.

Accelerated photostability tests. For accelerated stability measurements, we fabricated in air a film of silica-coated QDs by drop-casting a QD solution onto a coverslip. To protect QDs from direct exposure to oxygen, the film was loaded into a customized airtight cuvette under a N$_2$ atmosphere (H$_2$O and O$_2$ below 1 ppm) in a glove box.

In the rapid-ageing test, the QD film was exposed to 462-nm light from a blue LED (LP462-MF1W, Thorlabs); the power incident onto the sample surface was 1.57 W cm^{-2}. The optical density of the QD film at the excitation wavelength was 1.24, and hence, the absorbed power was 1.48 W cm^{-2}. On the basis of the experimentally measured QD absorption spectrum, the same film would absorb 6 mW cm^{-2} under 1 sun conditions. The above values indicate that in the case of LED excitation the 'acceleration' factor (F_A) was 247.

The PL QY of the film was recorded at 25 h intervals, as shown in Fig. 3b. According to these measurements, virtually no changes in the PL QY occurs up to ~100 h of exposure to high-intensity LED light. Then, we observe a slight decline in the emission intensity; however, 91% of the original PL QY is still preserved at the completion of the 200 h test.

Given F_A = 247, the 200 h of accelerated ageing translates into 5.6 years of exposure to direct sunlight. Considering a day–night cycle and statistical weather variations, the actual longevity of our samples is even higher. For example, the annual amount of daylight in New Mexico is 3,468 h, which corresponds to an average daily amount of 9.5 h. Hence, 5.6 years of continuous exposure to sunlight would translate into ~14 year durability under realistic outdoor conditions. This level of stability is comparable to that required for commercial solar cells.

Thermal stability tests. In studies of thermal stability, spin-cast QD films were placed into an oven preheated to a desired temperature (50–200 °C) and then heated for 30 min in air. For temperatures up to 50 °C, both silica-coated (5-nm shell thickness) and uncoated QDs did not show any signatures of PL degradation (Fig. 3c). However, after treatment at 100 °C, the uncoated QDs lost ~20% of the original PL QY, while the PL QY of silica-coated QDs remained intact. The treatment at higher temperatures resulted in a progressively stronger PL quenching in films of uncoated QDs and the PL loss reached ~60% after the 200 °C treatment. On the other hand, no appreciable changes in the PL efficiency were observed for silica-coated dots for temperature up to 200 °C (Fig. 3c).

Fabrication of QD/polymer films. Silica-coated g-QDs dispersed in ethanol (40 mg ml^{-1}; the weight of silica shell was not included) were mixed with a PVP solution (0.6 g ml^{-1} in ethanol) to form a homogeneous g-QD/polymer slurry of appropriate viscosity. To obtain a high-quality film, the slurry was centrifuged to remove any bubbles. In the film fabrication process, the g-QD/polymer mixture is placed on a glass substrate behind a blade (Fig. 4a). The blade is translated over the substrate at a constant speed, leaving behind a viscous QD/polymer layer, which turns into a highly uniform and transparent film after evaporation of ethanol. The QD/PVP films were deposited using either a manual version of a doctor-blade technique or a commercial doctor-blade apparatus (MTI Corporation, MSK-AFA-L800). Adjusting the size of the gap between the blade and the substrate allows for controlling the film thickness. According to previous reports, the final thickness of the dried film depends on the viscosity of the slurry and the blade-translation speed[39]. In our studies the gap was fixed at 100 μm, and the resulting film thickness (d) was ~50 μm.

LSC performance characteristics. We use several characteristics to quantify the LSC performance. We define the PL QY of an LSC ($\eta_{PL,LSC}$) as the ratio between the total number of photons emitted by the LSC and number of photons absorbed by it. Importantly, the PL QY introduced in this way may differ from the 'intrinsic' PL QY of the QDs (η_{PL}) measured for dilute QD solutions due to LSC-specific processes such as reabsorption of guided light followed by non-radiative recombination. We further introduce the edge-emission efficiency (η_{edge}) defined as the ratio between the number of photons emitted from the LSC edges and the total number of photons emitted from all LSC surfaces. For a waveguide with the refractive index of 1.5, the maximum value of η_{edge} is ~75%; the remaining 25% of photons leave the LSC through a so-called 'escape cone' defined by the angle of total internal reflection[42]. In a non-ideal case, the value of η_{edge} is reduced due to non-radiative recombination in LSC fluorophores as well as additional losses through the escape cone following reabsorption/re-emission events and scattering of guided light in a polymer matrix and an underlying substrate. The internal quantum efficiency (η_{int}) or collection efficiency (η_{col}) is defined as the ratio of the number of photons collected at the LSC edges and the number of incident photons absorbed by the LSC. It can be calculated from $\eta_{int} = \eta_{col} = \eta_{PL,LSC}\,\eta_{edge}$. The external quantum efficiency (η_{ext}) can be obtained by multiplying η_{int} by the LSC absorptance, $\eta_{abs} = (1 - R)(1 - 10^{-OD})$, which yields $\eta_{ext} = \eta_{abs}\,\eta_{int} = (1 - R)(1 - 10^{-OD})\eta_{PL,LSC}\,\eta_{edge}$; R and OD are, respectively, the reflectance and the optical density of the LSC at the incident-light wavelength. Finally, we introduce the concentration factor (C), which is defined as the ratio of flux densities of outcoupled and incident radiation. This quantity can be thought of as an effective enlargement (or contraction) factor of an area of a PV device when it is coupled to an LSC. The C-factor is related to η_{ext} by $C = G\eta_{ext}$, where G is the geometric gain factor (the ratio of the areas of the front surface and device edges), which for the studied devices can be found from $G = L/[4(D + d)]$ (Fig. 4a).

References

1. Debije, M. G. & Verbunt, P. P. C. Thirty years of luminescent solar concentrator research: solar energy for the built environment. *Adv. Energy Mater.* **2**, 12–35 (2012).
2. Sark, W. G. J. H. M. v. *et al.* Luminescent solar concentrators—a review of recent results. *Opt. Express* **16**, 21773–21792 (2008).
3. Chemisana, D. Building integrated concentrating photovoltaics: a review. *Renew. Sustain. Energy Rev.* **15**, 603–611 (2011).
4. Leow, S. W., Corrado, C., Osborn, M. & Carter, S. A. High and low concentrator systems for solar electric applications VIII. *Proc. SPIE* **8821**, 882103 (2013).
5. Klimov, V. I., Baker, T. A., Lim, J., Velizhanin, K. A. & McDaniel, H. Quality factor of luminescent solar concentrators and practical concentration limits attainable with semiconductor quantum dots. *ACS Photon.* **3**, 1138–1148 (2016).
6. Zhao, Y. & Lunt, R. R. Transparent luminescent solar concentrators for large-area solar windows enabled by massive Stokes-shift nanocluster phosphors. *Adv. Energy Mater.* **3**, 1143–1148 (2013).
7. Purcell-Milton, F. & Gun'ko, Y. K. Quantum dots for luminescent solar concentrators. *J. Mater. Chem.* **22**, 16687–16697 (2012).
8. Kim, J. Y., Voznyy, O., Zhitomirsky, D. & Sargent, E. H. 25th anniversary article: colloidal quantum dot materials and devices: a quarter-century of advances. *Adv. Mater.* **25**, 4986–5010 (2013).
9. Meinardi, F. *et al.* Large-area luminescent solar concentrators based on 'Stokes-shift-engineered' nanocrystals in a mass-polymerized PMMA matrix. *Nat. Photon.* **8**, 392–399 (2014).
10. Bradshaw, L. R., Knowles, K. E., McDowall, S. & Gamelin, D. R. Nanocrystals for luminescent solar concentrators. *Nano Lett.* **15**, 1315–1323 (2015).
11. Erickson, C. S. *et al.* Zero-reabsorption doped-nanocrystal luminescent solar concentrators. *ACS Nano* **8**, 3461–3467 (2014).
12. Meinardi, F. *et al.* Highly efficient large-area colourless luminescent solar concentrators using heavy-metal-free colloidal quantum dots. *Nat. Nanotech.* **10**, 878–885 (2015).
13. Krumer, Z. *et al.* Tackling self-absorption in luminescent solar concentrators with type-II colloidal quantum dots. *Sol. Energy Mater. Sol. Cells* **111**, 57–65 (2013).
14. Knowles, K. E., Kilburn, T. B., Alzate, D. G., McDowall, S. & Gamelin, D. R. Bright CuInS$_2$/CdS nanocrystal phosphors for high-gain full-spectrum luminescent solar concentrators. *Chem. Commun.* **51**, 9129–9132 (2015).
15. Li, C. *et al.* Large Stokes shift and high efficiency luminescent solar concentrator incorporated with CuInS$_2$/ZnS quantum dots. *Sci. Rep.* **5**, 17777 (2015).
16. Gallagher, S. J., Norton, B. & Eames, P. C. Quantum dot solar concentrators: electrical conversion efficiencies and comparative concentrating factors of fabricated devices. *Sol. Energy* **81**, 813–821 (2007).
17. Ma, Y. *et al.* Bulk synthesis of homogeneous and transparent bulk core/multishell quantum dots/PMMA nanocomposites with bright luminescence. *J. Appl. Polym. Sci.* **130**, 1548–1553 (2013).
18. Coropceanu, I. & Bawendi, M. G. Core/shell quantum dot based luminescent solar concentrators with reduced reabsorption and enhanced efficiency. *Nano Lett.* **14**, 4097–4101 (2014).
19. Lee, J., Sundar, V. C., Heine, J. R., Bawendi, M. G. & Jensen, K. F. Full color emission from II–VI semiconductor quantum dot–polymer composites. *Adv. Mater.* **12**, 1102–1105 (2000).
20. Walker, G. W. *et al.* Quantum-dot optical temperature probes. *Appl. Phys. Lett.* **83**, 3555–3557 (2003).
21. Bronstein, N. D. *et al.* Luminescent solar concentration with semiconductor nanorods and transfer-printed micro-silicon solar cells. *ACS Nano* **8**, 44–53 (2014).
22. Bae, W. K., Brovelli, S. & Klimov, V. I. Spectroscopic insights into the performance of quantum dot light-emitting diodes. *MRS Bull.* **38**, 721–730 (2013).
23. Koike, Y., Tanio, N. & Ohtsuka, Y. Light scattering and heterogeneities in low-loss poly(methyl methacrylate) glasses. *Macromolecules* **22**, 1367–1373 (1989).
24. Koczkur, K. M., Mourdikoudis, S., Polavarapu, L. & Skrabalak, S. E. Polyvinylpyrrolidone (PVP) in nanoparticle synthesis. *Dalton Trans.* **44**, 17883–17905 (2015).
25. Lim, J. *et al.* Influence of shell thickness on the performance of light-emitting devices based on CdSe/Zn$_{1-x}$Cd$_x$S core/shell heterostructured quantum dots. *Adv. Mater.* **26**, 8034–8040 (2014).
26. Piryatinski, A., Ivanov, S. A., Tretiak, S. & Klimov, V. I. Effect of quantum and dielectric confinement on the exciton-exciton interaction energy in type II core/shell semiconductor nanocrystals. *Nano Lett.* **7**, 108–115 (2007).

27. García-Santamaría, F. *et al.* Suppressed Auger recombination in 'giant' nanocrystals boosts optical gain performance. *Nano Lett.* **9**, 3482–3488 (2009).

28. García-Santamaría, F. *et al.* Breakdown of volume scaling in Auger recombination in CdSe/CdS heteronanocrystals: the role of the core–shell interface. *Nano Lett.* **11**, 687–693 (2011).

29. Brovelli, S. *et al.* Nano-engineered electron–hole exchange interaction controls exciton dynamics in core–shell semiconductor nanocrystals. *Nat. Commun.* **2**, 280 (2011).

30. Bae, W. K. *et al.* Controlled alloying of the core–shell interface in CdSe/CdS quantum dots for suppression of Auger recombination. *ACS Nano* **7**, 3411–3419 (2013).

31. Darbandi, M., Thomann, R. & Nann, T. Single quantum dots in silica spheres by microemulsion synthesis. *Chem. Mater.* **17**, 5720–5725 (2005).

32. Hu, X. & Gao, X. Silica-polymer dual layer-encapsulated quantum dots with remarkable stability. *ACS Nano* **4**, 6080–6086 (2010).

33. Aubert, T. *et al.* Bright and stable CdSe/CdS@SiO$_2$ nanoparticles suitable for long-term cell labeling. *ACS Appl. Mater. Interfaces* **6**, 11714–11723 (2014).

34. Xu, Y., Lian, J., Mishra, N. & Chan, Y. Multifunctional semiconductor nanoheterostructures via site-selective silica encapsulation. *Small* **9**, 1908–1915 (2013).

35. Hutter, E. M. *et al.* Method to incorporate anisotropic semiconductor nanocrystals of all shapes in an ultrathin and uniform silica shell. *Chem. Mater.* **26**, 1905–1911 (2014).

36. Koole, R. *et al.* On the incorporation mechanism of hydrophobic quantum dots in silica spheres by a reverse microemulsion method. *Chem. Mater.* **20**, 2503–2512 (2008).

37. Yang, P., Ando, M. & Murase, N. Highly luminescent CdSe/Cd$_x$Zn$_{1-x}$S quantum dots coated with thickness-controlled SiO$_2$ shell through silanization. *Langmuir* **27**, 9535–9540 (2011).

38. Wengeler, L., Schmitt, M., Peters, K., Scharfer, P. & Schabel, W. Comparison of large scale coating techniques for organic and hybrid films in polymer based solar cells. *Chem. Eng. Process.* **68**, 38–44 (2013).

39. Meeks, K., Pantoya, M. L. & Apblett, C. Deposition and characterization of energetic thin films. *Combust. Flame* **161**, 1117–1124 (2014).

40. Suzuki, K. *et al.* Reevaluation of absolute luminescence quantum yields of standard solutions using a spectrometer with an integrating sphere and a back-thinned CCD detector. *Phys. Chem. Chem. Phys.* **11**, 9850–9860 (2009).

41. Wurth, C., Grabolle, M., Pauli, J., Spieles, M. & Resch-Genger, U. Comparison of methods and achievable uncertainties for the relative and absolute measurement of photoluminescence quantum yields. *Anal. Chem.* **83**, 3431–3439 (2011).

42. Bomm, J. *et al.* Fabrication and full characterization of state-of-the-art quantum dot luminescent solar concentrators. *Sol. Energy Mater. Sol. Cells* **95**, 2087–2094 (2011).

43. Kagan, C. R., Murray, C. B., Nirmal, M. & Bawendi, M. G. Electronic energy transfer in CdSe quantum dot solids. *Phys. Rev. Lett.* **76**, 1517–1520 (1996).

Author contributions

J.L. fabricated and characterized the QD samples. H.L. developed the procedure for QD overcoating with silica and conducted characterization of the resulting QD/silica structures. H.L. and K.W. fabricated devices using a doctor-blade approach. K.W. characterized and analysed their LSC performance. H.-J.S. fabricated and characterized coupled LSC–PV devices. V.I.K. initiated the study, developed the analytical LSC model, and wrote the manuscript with contributions from all co-authors. H.L. and K.W. contributed equally to this work.

Additional information

Supplementary information is available for this paper. Reprints and permissions information is available at www.nature.com/reprints. Correspondence and requests for materials should be addressed to V.I.K.

Competing interests

The authors declare no competing financial interests.